WestVirginiaUniversity
THE RESEARCH REPOSITORY @ WVU

Faculty Scholarship

2016

Identification of photocurrents in topological insulators

Derek A. Bas
West Virginia University

Rodrigo A. Muniz
University of Toronto

Sercan Babakiray
West Virginia University

David Lederman
West Virginia University

J. E. Sipe
University of Toronto

See next page for additional authors

Follow this and additional works at: https://researchrepository.wvu.edu/faculty_publications

Part of the Optics Commons

Authors

Derek A. Bas, Rodrigo A. Muniz, Sercan Babakiray, David Lederman, J. E. Sipe, and Alan D. Bristow

Identification of photocurrents in topological insulators

DEREK A. BAS,[1] RODRIGO A. MUNIZ,[2] SERCAN BABAKIRAY,[1] DAVID LEDERMAN,[1] J. E. SIPE,[2] AND ALAN D. BRISTOW[1,*]

[1]*Department of Physics and Astronomy, West Virginia University, Morgantown, WV 26506-6315, USA*
[2]*Department of Physics and Institute of Optical Sciences, University of Toronto, Toronto, Ontario M5S 1A7, Canada*
[*]*alan.bristow@mail.wvu.edu*

Abstract: Optical injection and detection of charge currents is an alternative to conventional transport and photoemission measurements, avoiding the necessity of invasive contact that may disturb the system being examined. This is a particular concern for analyzing the surface states of topological insulators. In this work one- and two-color sources of photocurrents are isolated and examined in epitaxial thin films of Bi_2Se_3. We demonstrate that optical excitation and terahertz detection simultaneously captures one- and two-color photocurrent contributions, which has not been required for other material systems. A method is devised to extract the two components, and in doing so each can be related to surface or bulk excitations through symmetry. The separation of such photocurrents in topological insulators opens a new avenue for studying these materials by all-optical methods.

© 2016 Optical Society of America

References and links

1. M. Z. Hasan and C. L. Kane, "Colloquium: Topological insulators," Rev. Mod. Phys. **82**, 3045–3067 (2010).
2. P. Hosur, "Circular photogalvanic effect on topological insulator surfaces: Berry-curvature-dependent response," Phys. Rev. B **83**, 035309 (2011).
3. S. K. Mishra, S. Satpathy, and O. Jepsen, "Electronic structure and thermoelectric properties of bismuth telluride and bismuth selenide," J. Phys.: Condens. Matter **9**, 461 (1997).
4. Y. S. Hor, A. Richardella, P. Roushan, Y. Xia, J. G. Checkelsky, A. Yazdani, M. Z. Hasan, N. P. Ong, and R. J. Cava, "p-type Bi_2Se_3 for topological insulator and low-temperature thermoelectric applications," Phys. Rev. B **79**, 195208 (2009).
5. D. Hsieh, J. W. McIver, D. H. Torchinsky, D. R. Gardner, Y. S. Lee, and N. Gedik, "Nonlinear optical probe of tunable surface electrons on a topological insulator," Phys. Rev. Lett. **106**, 057401 (2011).
6. N. Kumar, B. A. Ruzicka, N. P. Butch, P. Syers, K. Kirshenbaum, J. Paglione, and H. Zhao, "Spatially resolved femtosecond pump-probe study of topological insulator Bi_2Se_3," Phys. Rev. B **83**, 235306 (2011).
7. P. Di Pietro, F. M. Vitucci, D. Nicoletti, L. Baldassarre, P. Calvani, R. Cava, Y. S. Hor, U. Schade, and S. Lupi, "Optical conductivity of bismuth-based topological insulators," Phys. Rev. B **86**, 045439 (2012).
8. R. Valdés Aguilar, A. V. Stier, W. Liu, L. S. Bilbro, D. K. George, N. Bansal, L. Wu, J. Cerne, A. G. Markelz, S. Oh, and N. P. Armitage, "Terahertz response and colossal Kerr rotation from the surface states of the topological insulator Bi_2Se_3," Phys. Rev. Lett. **108**, 087403 (2012).
9. Y. D. Glinka, S. Babakiray, T. A. Johnson, A. D. Bristow, M. B. Holcomb, and D. Lederman, "Ultrafast carrier dynamics in thin-films of the topological insulator Bi_2Se_3," Appl. Phys. Lett. **103**, 151903 (2013).
10. S. Lu, C. Zhao, Y. Zou, S. Chen, Y. Chen, Y. Li, H. Zhang, S. Wen, and D. Tang, "Third order nonlinear optical property of Bi_2Se_3," Opt. Express **21**, 2072–2082 (2013).
11. J. W. McIver, D. Hsieh, H. Steinberg, P. Jarillo-Herrero, and N. Gedik, "Control over topological insulator photocurrents with light polarization," Nat. Nanotechnol. **7**, 96–100 (2012).
12. S. Sim, M. Brahlek, N. Koirala, S. Cha, S. Oh, and H. Choi, "Ultrafast terahertz dynamics of hot Dirac-electron surface scattering in the topological insulator Bi_2SeS3," Phys. Rev. B **89**, 165137 (2014).
13. J. W. McIver, D. Hsieh, S. G. Drapcho, D. H. Torchinsky, D. R. Gardner, Y. S. Lee, and N. Gedik, "Theoretical and experimental study of second harmonic generation from the surface of the topological insulator Bi_2Se_3," Phys. Rev. B **86**, 035327 (2012).
14. L. Fu and C. L. Kane, "Superconducting proximity effect and Majorana fermions at the surface of a topological insulator," Phys. Rev. Lett. **100**, 096407 (2008).

15. J. Wang, H. Mabuchi, and X.-L. Qi, "Calculation of divergent photon absorption in ultrathin films of a topological insulator," Phys. Rev. B **88**, 195127 (2013).
16. J. Seo, P. Roushan, H. Beidenkopf, Y. S. Hor, R. J. Cava, and A. Yazdani, "Transmission of topological surface states through surface barriers," Nature **466**, 343–346 (2010).
17. D. Galanakis and T. D. Stanescu, "Electrostatic effects and band bending in doped topological insulators," Phys. Rev. B **86**, 195311 (2012).
18. F. Nastos and J. E. Sipe, "Optical rectification and shift currents in GaAs and GaP response: Below and above the band gap," Phys. Rev. B **74**, 035201 (2006).
19. D. Côté, N. Laman, and H. M. v. Driel, "Rectification and shift currents in GaAs," Appl. Phys. Lett. **80**, 905–907 (2002).
20. N. Laman, M. Bieler, and H. M. v. Driel, "Ultrafast shift and injection currents observed in wurtzite semiconductors via emitted terahertz radiation," J. Appl. Phys. **98**, 103507 (2005).
21. F. Nastos and J. E. Sipe, "Optical rectification and current injection in unbiased semiconductors," Phys. Rev. B **82**, 235204 (2010).
22. M. Bieler, K. Pierz, and U. Siegner, "Simultaneous generation of shift and injection currents in (110)-grown GaAs/AlGaAs quantum wells," J. Appl. Phys. **100**, 083710 (2006).
23. L. Costa, M. Betz, M. Spasenović, A. D. Bristow, and H. M. van Driel, "All-optical injection of ballistic electrical currents in unbiased silicon," Nat. Phys. **3**, 632–635 (2007).
24. A. Haché, Y. Kostoulas, R. Atanasov, J. L. P. Hughes, J. E. Sipe, and H. M. van Driel, "Observation of coherently controlled photocurrent in unbiased, bulk GaAs," Phys. Rev. Lett. **78**, 306–309 (1997).
25. D. Sun, C. Divin, J. Rioux, J. E. Sipe, C. Berger, W. A. de Heer, P. N. First, and T. B. Norris, "Coherent control of ballistic photocurrents in multilayer epitaxial graphene using quantum interference," Nano Lett. **10**, 1293–1296 (2010).
26. R. A. Muniz and J. E. Sipe, "Coherent control of optical injection of spin and currents in topological insulators," Phys. Rev. B **89**, 205113 (2014).
27. D. A. Bas, K. Vargas-Velez, S. Babakiray, T. A. Johnson, P. Borisov, T. D. Stanescu, D. Lederman, and A. D. Bristow, "Coherent control of injection currents in high-quality films of Bi_2Se_3," Appl. Phys. Lett. **106**, 041109 (2015).
28. J. A. Sobota, S.-L. Yang, A. F. Kemper, J. J. Lee, F. T. Schmitt, W. Li, R. G. Moore, J. G. Analytis, I. R. Fisher, P. S. Kirchmann, T. P. Devereaux, and Z.-X. Shen, "Direct optical coupling to an unoccupied Dirac surface state in the topological insulator Bi_2Se_3," Phys. Rev. Lett. **111**, 136802 (2013).
29. P. Olbrich, L. Golub, T. Herrmann, S. Danilov, H. Plank, V. Bel'kov, G. Mussler, C. Weyrich, C. Schneider, J. Kampmeier, D. Grützmacher, L. Plucinski, M. Eschbach, and S. Ganichev, "Room-Temperature High-Frequency Transport of Dirac Fermions in Epitaxially Grown Sb_2Te_3- and Bi_2Te_3-Based Topological Insulators," Phys. Rev. Lett. **113**, 096601 (2014).
30. L.-G. Zhu, B. Kubera, K. Fai Mak, and J. Shan, "Effect of Surface States on Terahertz Emission from the Bi_2Se_3 Surface," Sci. Rep. **5**, 10308 (2015).
31. L. Braun, G. Mussler, A. Hruban, M. Konczykowski, M. Wolf, T. Schumann, M. Münzenberg, L. Perfetti, and T. Kampfrath, "Ultrafast photocurrents at the surface of the three-dimensional topological insulator Bi_2Se_3," arXiv:1511.00482 [cond-mat] (2015). arXiv: 1511.00482.
32. C. Ruppert, J. Lohrenz, S. Thunich, and M. Betz, "Ultrafast field-resolved semiconductor spectroscopy utilizing quantum interference control of currents," Opt. Lett. **37**, 3879–3881 (2012).
33. P. Tabor, C. Keenan, S. Urazhdin, and D. Lederman, "Molecular beam epitaxy and characterization of thin Bi_2Se_3 films on Al_2O_3 (110)," Appl. Phys. Lett. **99**, 013111 (2011).
34. Y. Zhang, K. He, C.-Z. Chang, C.-L. Song, L.-L. Wang, X. Chen, J.-F. Jia, Z. Fang, X. Dai, W.-Y. Shan, S.-Q. Shen, Q. Niu, X.-L. Qi, S.-C. Zhang, X.-C. Ma, and Q.-K. Xue, "Crossover of the three-dimensional topological insulator Bi_2Se_3 to the two-dimensional limit," Nat. Phys. **6**, 584–588 (2010).
35. D. Côté, J. E. Sipe, and H. M. van Driel, "Simple method for calculating the propagation of terahertz radiation in experimental geometries," J. Opt. Soc. Am. B **20**, 1374–1385 (2003).
36. J. D. Rowley, J. K. Pierce, A. T. Brant, L. E. Halliburton, N. C. Giles, P. G. Schunemann, and A. D. Bristow, "Broadband terahertz pulse emission from $ZnGeP_2$," Opt. Lett. **37**, 788–790 (2012).
37. D. Grischkowsky, S. Keiding, M. van Exter, and C. Fattinger, "Far-infrared time-domain spectroscopy with terahertz beams of dielectrics and semiconductors," J. Opt. Soc. Am. B **7**, 2006–2015 (1990).
38. C. Sames, J.-M. Ménard, M. Betz, A. L. Smirl, and H. M. van Driel, "All-optical coherently controlled terahertz ac charge currents from excitons in semiconductors," Phys. Rev. B **79**, 045208 (2009).
39. S. M. Harrel, R. L. Milot, J. M. Schleicher, and C. A. Schmuttenmaer, "Influence of free-carrier absorption on terahertz generation from ZnTe(110)," Journal of Applied Physics **107**, 033526 (2010).
40. H. Zhao, E. J. Loren, H. M. van Driel, and A. L. Smirl, "Coherence control of Hall charge and spin currents," Phys. Rev. Lett. **96**, 246601 (2006).
41. M. S. Bahramy, P. D. C. King, A. de la Torre, J. Chang, M. Shi, L. Patthey, G. Balakrishnan, P. Hofmann, R. Arita, N. Nagaosa, and F. Baumberger, "Emergent quantum confinement at topological insulator surfaces," Nat. Commun. **3**, 1159 (2012).
42. X. F. Kou, L. He, F. X. Xiu, M. R. Lang, Z. M. Liao, Y. Wang. A. V. Fedorov, X. X. Yu, J. S. Tang, G. Huang, X. W. Jiang, J. F. Zhu, J. Zou and K. L. Wang, "Epitaxial growth of high mobility Bi_2Se_3 thin films on Cds," App.

Phys. Lett. **98**, 242102 (2011).
43. F. Xiu, N. Meyer, X. Kou, L. He, M. Lang, Y. Wang, X. Yu, A. V. Federov, J. Zou and K. L. Wang, "Quantum capacitance in topological insulators," Sci. Rep. **2**, 669 (2012).
44. M. J. Stevens, A. L. Smirl, R. D. R. Bhat, A. Najmaie, J. E. Sipe, and H. M. van Driel, "Quantum interference control of ballistic pure spin currents in semiconductors," Phys. Rev. Lett. **90**, 136603 (2003).

1. Introduction

A topological insulator (TI) has robust Dirac surface states (SS) that are immune from back-scattering by non-magnetic impurities, exhibiting helical spin texture [1,2]. Bi_2Se_3 is a prototypical three-dimensional TI that has been intensively studied for its electronic, thermoelectric [3,4], and optical properties [5–13]. As-grown Bi_2Se_3 is n-type material due to selenium vacancies, which complicates transport measurements associated with the SS. Additionally, many surface effects arise due to interfaces between TIs and other materials, some of which can lead to exotic phenomena [14–17]. All-optical photocurrent measurements are non-invasive, overcoming the need for contacts while studying the intricacies of the charge carrier dynamics from the topological SS.

Several "one-color photocurrents" arise in simple semiconductors, such as in non-centrosymmetric zincblende GaAs, due to excitation with pulsed laser light. Photon energies $\hbar\omega$ below the band gap E_g excite optical rectification, where the induced dipole moment per unit volume follows the intensity of the pulse. For $\hbar\omega > E_g$, a real-space change in the charge distribution between the valence and conduction band leads to a shift current [18,19], where the current density follows the intensity of the pulse. Above band-gap excitation of lower symmetry semiconductors, such as wurtzite crystals, results in electrons and holes being injected preferentially on one side of the Brillouin zone [20]. The rate of change of this injection current density follows the intensity of the pulse. One-color optical rectification, shift currents, and injection currents are all aspects of the second-order nonlinear optical response of non-centrosymmetric materials [21] and emit terahertz (THz) radiation. Shift and injection currents occur simultaneously for the correct sample symmetry [20,22] and are separable by analyzing the polarization dependence.

One-color photocurrents do not survive in centrosymmetric crystals, such as silicon. However, "two-color photocurrents" arise through quantum interference of single- and two-photon absorption between pulses with photon energies of $\hbar2\omega$ and $\hbar\omega$ respectively and lead to injection currents. The resulting injection current dominates when $2\hbar\omega > E_g$ and can be controlled by the relative phase ($\Delta\phi = \phi_{2\omega} - 2\phi_\omega$) of the two pulses. Two-color injection currents survive in all materials, for example in centrosymmetric silicon [23], non-centrosymmetric (100)-grown GaAs materials [24], and centrosymmetric graphene [25]. Other two-color photocurrents exist but typically injection currents are the largest if they survive, and if not shift currents are typically larger than the rectification currents.

Bismuth selenide (Bi_2Se_3) is a TI with a rich band structure, where two-color injection currents have been proposed [26] and observed using a THz probe [27]. Due to the relatively small band gap of Bi_2Se_3 (~0.3 eV), optoelectronic applications only involving topological SS had been thought to require optical fields with mid-to-far infrared frequencies. However, a second Dirac cone of surface states (SS2) was discovered at 1.7 eV above the commonly studied Dirac point (SS1) [28]. Consequently, surface-to-surface optical transitions can be excited between the Dirac cones, offering control with commercial NIR lasers [9,27]. Moreover, the centrosymmetry of bulk Bi_2Se_3 [5,11,29] leaves only one-color effects from the surface [29–31]. This situation means that both one-color surface and two-color surface and bulk photocurrents must be present in thin films of Bi_2Se_3. Pump-probe contributions, even outside of the cross-correlation envelope of the two excitation pulses, do not allow the one-color effects to be cleanly isolated [32]. Blocking either of the pump pulses does not provide the correct signal amplitude to then subtract one-color from the

total (one- and two-color) photocurrent signal. In this paper, one- and two-color photocurrents are separated by symmetry and phase dependence of the emitted THz radiation. Two-color signatures are confirmed to be injection currents by the phase dependence. One-color signals are associated with shift currents, because previous circular photogalvanic measurements eliminate photon drag due to spin degeneracy [11,29] and bulk optical rectification is only observed at non-normal incidence [30]. Separation allows for identification of surface and bulk contributions and estimates of their respective current densities. All-optical photocurrent identification schemes, such as the one presented here, can be applied to surface currents in any systems where both one- and two-color photocurrents are comparable in strength.
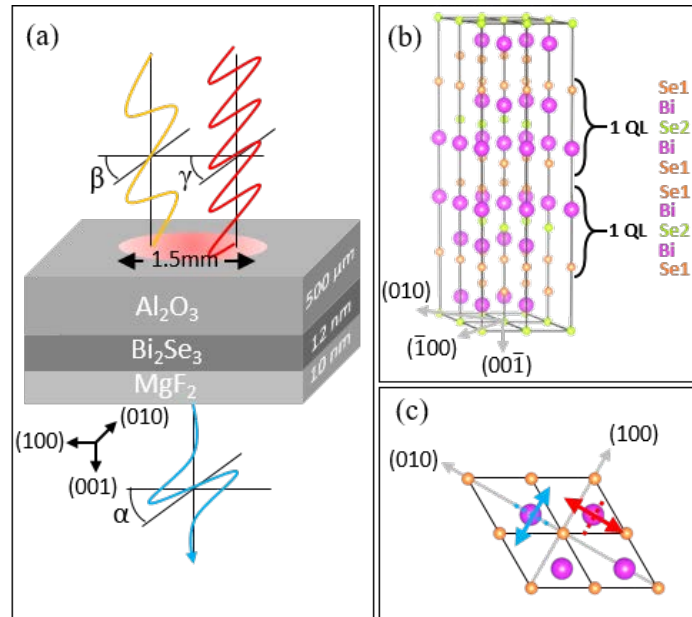

Fig. 1. (a) Schematic diagram of experimental configuration for the Bi_2Se_3 film on a sapphire substrate and MgF_2 capping layer. α, β and γ are the respective angles of the electric fields of the THz emission, ω pulse and 2ω pulse with respect to the (100) axis of the topological insulator. (b) Four unit cells, showing the trigonal symmetry of the Bi_2Se_3 lattice and the atomic layers that comprise a quintuple layer (QL). (c) Top-down view of one QL, with two examples of the pump polarization ($\beta = \gamma$). For the blue polarization, the lattice looks symmetric. For red polarization, the symmetry is broken and a directional shift current is expected. For $\alpha = \beta + \pi/2$, the relevant symmetry plane is along the direction of the polarization vector.

2. Experiment

Figure 1(a) shows a schematic representation of the sample. A 12-nm Bi_2Se_3 film is grown by molecular beam epitaxy on a sapphire substrate [27, 33]. A 10-nm MgF_2 capping layer prevents exposure to atmosphere and inhibits the build-up of a surface space charge field and the associated band bending [30, 31]. Both the substrate and capping layer are transparent to the optical radiation used in the experiment. Figure 1(b) shows four rhombohedral unit cells of the Bi_2Se_3, wherein the bismuth (Bi) and selenium (Se) layers alternate within a quintuple layer (QL). This results in Bi layers always being surrounded by Se layers, but Se layers take two identifiable positions: Se2 layers surrounded by Bi and Se1 layers forming the edge of each QL bonded to the adjacent QL by van der Waals bonds. The van der Waal bonds make Bi_2Se_3 easy to

cleave or exfoliate and form a building block for quasi-two-dimensional material structures. Due to the structure a 12-nm thick film has 12 QL and is sufficiently thick to prevent SS hybridization of the opposite surfaces of the sample [34].

Experiments use a laser amplifier and an optical parametric amplifier (OPA) to provide ~80-fs pulses at a repletion rate of 1 kHz. Pulses from the OPA centered at 1540 nm (0.8 eV) pump a β-barium borate crystal to generate second-harmonic pulses at 770 nm (1.6 eV) [27]. These fundamental (ω) and frequency-doubled (2ω) pulses feed a two-color Mach-Zehnder interferometer that allows for independent control of the intensity, phase, and polarization of the two pulses. Both colors emerge with linear polarization with fidelity confirmed by a linear polarizer with 10^{-4} extinction ratio. The average beam powers for ω and 2ω were approximately 35 mW and 1 mW respectively. Both beams were collimated and have $1/e^2$ diameters of approximately 1.5 mm at the sample position. The pulse combination impinges the sample at normal incidence. Acceleration of charge due to the production and decay of the photocurrent leads to THz radiation following the form dJ/dt [35]. THz emission is collected using off-axis parabolic mirrors and detected with electro-optic (EO) sampling. An 80-fs gate pulses is derived from the laser amplifier to record the THz emission in the time domain by varying the relative delay time t_{det}. The peak THz field produced by ω excitation is used to define $t_{det} = 0$. The delay time τ between the ω and 2ω pulses (and hence the phase parameter $\Delta\phi = \phi_{2\omega} - 2\phi_{\omega}$) is controlled by a pair of glass wedges in the two-color interferometer and $\tau = 0$ was identified with the point of maximum injection current within the cross-correlation of the two excitation pulses.

Figure 1(a) illustrates the generalized case for two pump pulses and THz emission where all three are linearly polarized. α, β and γ are the polarization angles of the electric field of the THz emission, ω pulse and 2ω pulses with respect to the (100) axis of the TI, but throughout this work $\beta = \gamma$. When the (100) axis is parallel with the pump polarization, β is set to zero. The orientation of the Bi_2Se_3 crystal lattice was confirmed by x-ray diffraction; however, a distinction is not made between (100) and ($\bar{1}$00) directions. β (and γ) is varied by the azimuthal rotation of the sample. α is varied for parallel ($\alpha = \beta$) and perpendicular ($\alpha = \beta + \pi/2$) polarization configurations by rotating the gate pulse polarization and the EO crystal together. The detection was calibrated using a strong OR source [36]. The ω and 2ω pulses transmitted through the substrate first before impinging the sample, which overcomes stretching of the THz emission by the substrate [37]. Optical phase walk-off of the pump pulses was corrected by the two-color interferometer. Measurements were performed rapidly to overcome phase drift, which was observed to be less than one cycle per hour.

3. Results and discussion

3.1. Shift and injection currents

A shift current can be induced by a single optical pump field $\hbar\omega > E_g$ or $2\hbar\omega > E_g$. The charge distribution in real space associated with a conduction band state is usually displaced from the charge distribution associated with the valence band state at the same position in the Brillouin zone; one charge distribution might be centered on the Bi atoms, and the other on the Se atoms, for example. During absorption, it is then possible for the charge distribution to evolve from that of the valence band state to that of the conduction band state in such a way that there is a net current associated with the change of state. This occurs most typically if the pump field vector points from one atom to the neighboring atom, shown by the red vector in Fig. 1(c). For the other polarization, shown by the blue vector, there is no preferred direction for the charge motion and no net shift current results.

The lowest order contribution to the shift current is governed by a third-rank tensor, and associated with a divergent part of $\chi^{(2)}$ [18, 21]. It can be computed in terms of the incident field

E_ω through a third-rank tensor ν_{abc} given by

$$J_a^{shift} = \nu_{abc} E_{-\omega}^b E_\omega^c + c.c. \tag{1}$$

The tensor ν_{abc} satisfies the same symmetries as the crystal lattice. It vanishes for centrosymmetric materials such as Bi_2Se_3, but inversion symmetry is broken at the surface and ν_{abc} can have non-vanishing components. For surface states in Bi_2Se_3, the only non-zero tensor component is ν_{xxx}. The parallel ($\alpha = \beta$) component of the current $J_\parallel$, and the perpendicular $\left(\alpha = \beta + \frac{\pi}{2}\right)$ component $J_\perp$ can be written as

$$\begin{aligned} J_\parallel^{shift} &= \nu_{xxx} \cos(3\beta) |E_\omega|^2, \\ J_\perp^{shift} &= -\nu_{xxx} \sin(3\beta) |E_\omega|^2. \end{aligned} \tag{2}$$

Similar terms exist for excitation with $|E_{2\omega}|^2$.

A two-color injection current uses two harmonically related pumps characterized by a phase parameter $\Delta\phi$, which overlap in time and space. The resulting quantum interference in momentum space produces an asymmetric distribution of excited electrons. The lowest order contribution to the injection current is associated with a divergent part of $\chi^{(3)}$, and governed by a fourth-rank tensor η_{abcd} given by

$$\frac{d}{dt} J_a^{inj} = \eta_{abcd} E_{-\omega}^b E_{-\omega}^c E_{2\omega}^d e^{i\Delta\phi} + c.c. \tag{3}$$

For both the surface and bulk of Bi_2Se_3, there are three independent components of η, namely η_{xxxx}, η_{xyyx} and η_{xyxy}. The injection rate of the current along the direction of the incident field ($\alpha = \beta$) is

$$\begin{aligned} \frac{d}{dt} J_\parallel^{inj} = \ &2[\mathrm{Re}\,(\eta_{xxxx}) \cos(\Delta\phi) \\ &+ \mathrm{Im}\,(\eta_{xxxx}) \sin(\Delta\phi)] |E_\omega|^2 |E_{2\omega}|, \end{aligned} \tag{4}$$

while the component of the injection current perpendicular to the incident field $\left(\alpha = \beta + \frac{\pi}{2}\right)$ vanishes $\frac{d}{dt} J_\perp^{inj} = 0$.

3.2. Observation of photocurrents

Figure 2 shows the THz emission from the Bi_2Se_3 versus t_{det} and $\Delta\phi$ for the parallel polarization configuration ($\alpha = \beta$). Both parts (a) and (b) show the total THz electric field measured for two-color excitation, which may include contributions from injection and/or shift currents depending on the polarization configuration and relative phase between the two color pulses. In (a), the excitation polarization is set to $\beta = \pi/6$, which corresponds to the blue vector in Fig. 1(c). As suspected, no one-color shift current is present and the relative phase dependence of the THz transients shows the familiar checkerboard pattern that results from a two-color injection current [23–25, 38]. At the appropriate relative phase conditions the photocurrent completely reverses, as shown in the inset for $\Delta\phi = \pi/2$ (gray) and $3\pi/2$ (white). Similar results are observed for excitation polarization conditions that correspond to $\beta = \pi/6 + n\pi/3$, where n is an integer.

In Fig. 2(b) excitation polarization is set to $\beta = 0$, corresponding to the red vector in Fig. 1(c). As for all $\beta = 0 + n\pi/3$, where n is an integer, the parallel component of the phase-dependent THz emission transients $E_\parallel^{THz}(\Delta\phi, t_{det})$ is altered due to the addition of one-color shift currents. Since an injection current is also generated, this means that for certain values of $\Delta\phi$ both shift and injection currents are observed simultaneously. Moreover, the injection current oscillates symmetrically with $\Delta\phi$, so integrating the THz transients over once complete cycle of relative phase will remove the injection current. The remaining signal in the THz transient is shown in the inset of Fig. 2(b) and corresponds only to the one-color photocurrents arising from ω and 2ω independently. This signal matches that observed for $\Delta\phi = 0$, where the injection current is zero; see Fig. 2(a).
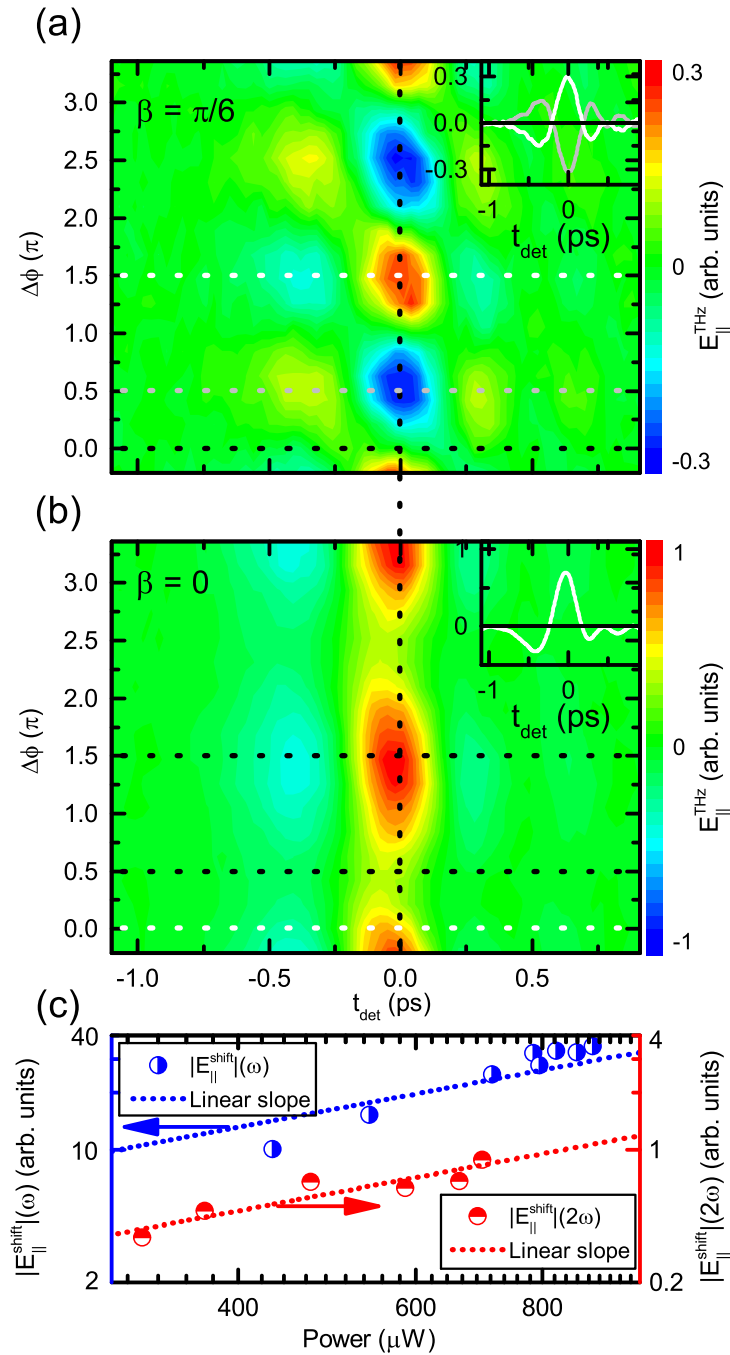
Fig. 2. Phase dependence of the emitted THz transients. $E_\parallel^{THz}(\Delta\phi, t_{det})$ is the parallel component of the THz field emitted from Bi_2Se_3 as a function of detection delay time and relative phase. (a) $\beta = \pi/6$ corresponds to the blue vector in Fig. 1(c), a geometry which suppresses shift current contributions. The resulting checkerboard pattern is characteristic of injection current [23]. The inset THz transients show complete reversal of the photocurrent between $\Delta\phi = \pi/2$ (gray) and $3\pi/2$ (white). (b) $\beta = 0$ corresponds to the red vector in Fig. 1(c), which allows for contributions from both shift and injection currents simultaneously. The inset transient is obtained by integrating one complete cycle of relative phase to show the remaining signal after removing the $\Delta\phi$ contribution. (c) Power dependence of the maximum electric field, recorded at $t_{det} = 0$ (vertical dotted line), for ω (left, blue) or 2ω (right, red) individually to confirm the nonlinear optical scaling associated with a shift current. The dotted lines are guides to the eye, showing a linear slope.

Power scaling of the injection current signal has been previously proved [27]. Figure 2(c) shows the average power dependence of the shift current signatures, namely the maximum in the parallel component of the THz transient measured at $t_{det} = 0$, $\beta = 0$ and $\Delta\phi = 0$, for ω (left,blue) and 2ω (right, red) excitation individually. Overall the 2ω shift current is an order of magnitude weaker than for ω excitation, predominantly due to the excitation irradiance. In both cases, increasing the average excitation power increases the THz electric field linearly, in accordance with Eq. (1) and confirming the second-order nonlinearity of the one-color processes. For the two-color pump conditions, the normalized THz electric field amplitudes corresponding to the two one-color shift currents are $E_\parallel^{THz}(\omega) = 1$ and $E_\parallel^{THz}(2\omega) = 0.26$, where $E_\parallel^{THz}(\omega + 2\omega) = 0.96$ when both pumps are present. Hence, simple addition of the two one-color shift current signals does not produce the total shift current in the presence of both excitation pulses and in a configuration where no injection current exists, implying that additional interactions occur. The reduction in signal also implies absorption effects, which must be studied without the presence of the injection current.

An injection current cross-correlation must be established. Figure 3(a) shows the relative-phase dependence of the injection current at the maximum of the THz transient ($t_{det} = 0$) and for $\beta = 0$ allowing a shift current offset. Data are fit with a cross-correlation envelope and sinusoidal phase-dependent injection current, $A \exp\left[-\frac{\tau^2}{0.36(\tau_x)^2}\right] \sin\left[\omega(\tau - \tau_0)\right] + 1$, where A is the magnitude, the center is $\tau = 0$ and the full width half maximum is $\tau_x = 0.28$ ps. With the envelope of the injection current established, a minute difference in the angles of incident (estimated to be ~0.015) between the two pulses is introduced by the Mach-Zehnder interferometer, while retaining maximum spatial overlap on the samples. Phase-front matching required for coherent emission due to the injection current is destroyed and non-radiative two-beam effects can be examined throughout and beyond the cross-correlation envelope. Figure 3(b) shows $E_\parallel^{shift}(2\omega, \tau)$ transients excited by 2ω alone, recorded at τ = -3.2 ps, -0.3 ps and 0.7 ps, color coded to the vertical lines in (a). For comparison, each of the three panels in (b) show the shift current produced by ω excitation alone $E_\parallel^{shift}(\omega)$ (red dotted line) and is used to define the zero delay time. Also shown, the $E_\parallel^{shift}(\omega)$ contribution is reduced by approximately 20% when the 2ω pulse impinges the sample 3.2 ps (~40 pulse widths) before the ω pulse. This reduction steadily increases to 50% as τ approaches 0 ps from negative values, but the emission returns to normal at $\tau > 0$ and a separate THz emission peak arises as the delay is increases to positive values. Such behavior is indicative of a pump-probe response and is revealed when plotting the normalized change in THz emission versus $-\tau$ at $\tau_{det} = 0$ ps; see Fig. 3(c). Photocarriers are excited by the 2ω pulse, leading to increased free-carrier conductivity and a reduction of the THz produced by the ω pulse [39]. Negative τ values of the pump-probe transient are fit with a pulse model of the form $\alpha\left[1 - \exp\left(-\frac{\tau - \tau_0}{\tau_1}\right)\right]^\beta \exp\left[-\frac{\tau - \tau_0}{\tau_2}\right]$, where the rise time $\tau_1 = 0.06$ ps and decay time $\tau_2 = 4.09$ s; α and β are arbitrary fitting parameters to match the signal strength.

3.3. Separation of photocurrents

The total current measured by the THz probe is a sum of both one-color shift currents and the two-color injection current. Injection currents depend on $\Delta\phi$ and shift currents do not. On the other hand, shift currents depend on polarization and injection currents do not. These facts can be exploited to separate the contributions *in situ*, namely with simultaneous excitation by both pulses. Since $J_\parallel^{inj}\left(\Delta\phi = \frac{\pi}{2}\right) = -J_\parallel^{inj}\left(\Delta\phi = \frac{3\pi}{2}\right)$, if the total current is measured for both values of the phase parameter

$$
\begin{aligned}
J_\parallel^{total}\left(\Delta\phi = \tfrac{\pi}{2}\right) &= J_\parallel^{shift} + J_\parallel^{inj}\left(\Delta\phi = \tfrac{\pi}{2}\right), \\
J_\parallel^{total}\left(\Delta\phi = \tfrac{3\pi}{2}\right) &= J_\parallel^{shift} + J_\parallel^{inj}\left(\Delta\phi = \tfrac{3\pi}{2}\right),
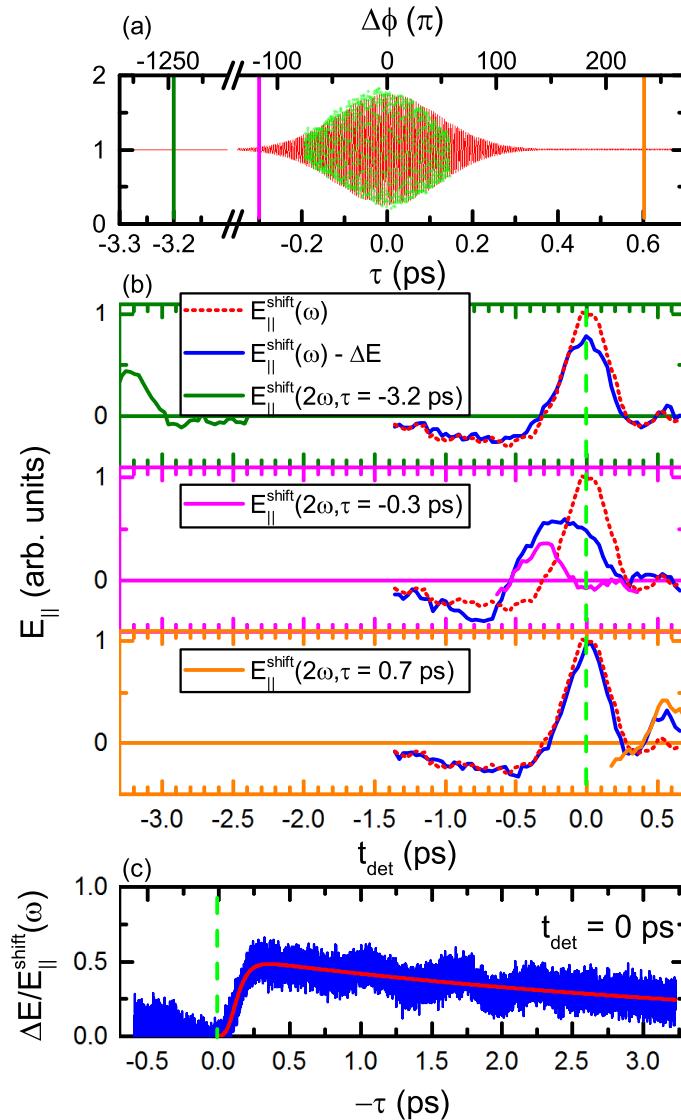\end{aligned}
\tag{5}
$$

Fig. 3. Transient response of one- and two-color excitation. (a) Injection current versus τ, defined by the sinusoidal phase dependence and cross-correlation window. (b) One- and two-color THz transients versus τ_{det}. $E_{\parallel}^{shift}(2\omega)$ is plotted for τ = -3.2 ps, -0.3 ps and 0.7 ps [coded by the color of vertical lines in (a)], $E_{\parallel}^{shift}(\omega,\tau)$ (red dotted line) is shown for comparison, and the two-color $E_{\parallel}^{shift}(\omega,\tau) - \Delta E$ shows the modification of the emission from ω due to the presence of 2ω. (c) Optical pump and THz probe [$\Delta E/E_{\parallel}^{shift}(\omega)$] versus τ at τ_{det} = 0, due to free-carrier absorption by carriers promoted by the 2ω pulse.
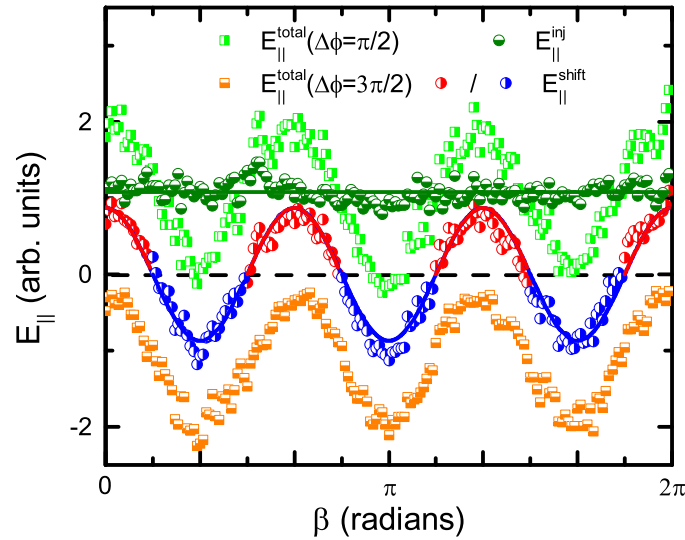
Fig. 4. Photocurrent separation analysis based on Eq. (6). Two-color excitation of photocurrent versus β, recording the maximum THz emission at $\tau_{det} = 0$ for relative phase conditions $\Delta\phi = \pi/2$ (green) and $3\pi/2$ (orange). Addition and subtraction of these two signals gives the shift current E^{shift} (blue for positive, red for negative) and injection current E^{inj} (olive) respectively. Solid lines are the theoretical model for E^{shift} and E^{inj}, fit to experimental amplitudes.

it is possible to extract both the injection and shift currents as

$$
\begin{aligned}
J_{\parallel}^{inj}\left(\tfrac{\pi}{2}\right) &= \tfrac{1}{2}\left[J_{\parallel}^{total}\left(\tfrac{\pi}{2}\right) - J_{\parallel}^{total}\left(\tfrac{3\pi}{2}\right)\right], \\
J_{\parallel}^{shift} &= \tfrac{1}{2}\left[J_{\parallel}^{total}\left(\tfrac{\pi}{2}\right) + J_{\parallel}^{total}\left(\tfrac{3\pi}{2}\right)\right].
\end{aligned}
\tag{6}
$$

Fig. 4 demonstrates the above treatment by showing the maximum of the parallel polarized THz emission ($\tau_{det} = 0$), recorded with both pulses exciting the sample at normal incidence, as a function of β for $\Delta\phi = \pi/2$ (green) and $3\pi/2$ (orange). The sum and difference of these signals reveals the shift current oscillating around zero field (blue for positive, red for negative) and the β-independent injection current (olive green). This method is similar to integrating with respect to phase to remove the injection current contribution which oscillated equally positive and negative about zero within the range between 0 and 2π. Similar is true for integrating with respect to polarization angle to remove the shift current. Experimental values have an error of ∼4.2% determined by fitting the extracted angle dependences to Eq. (6).

3.4. Surface and bulk currents

Comparison of one-color and two-color excitation of photocurrents can be used to distinguish the surface and bulk contributions of TI film. Figure 5 shows the maximum THz emission ($t_{det} = 0$) for ω excitation as a function of crystal orientation β for (a) parallel ($\alpha = \beta$) and (b) perpendicular ($\alpha = \beta + \pi/2$) polarization configurations. Both measurements reflect the three-fold symmetry of the surface as described in Eq. (2), yielding three positive (red) and three negative (blue) lobes. Shift currents due to 2ω excitation (not shown) exhibit the same symmetry, but are significantly weaker due to the average excitation power and the absorption coefficients. Good agreement is found between and experiment and theory for $E_{\parallel}^{shift}$ and $E_{\perp}^{shift}$, where only the amplitudes are free parameters. The amplitudes of both polarization configurations (excited

with the same color) are equal within the experimental uncertainty and the ω value serves as the reference for comparing the two-color contributions shown in Figs. 5(c) and 5(d).

Using Eq. (6), the shift (blue for positive, red for negative) and injection (green) currents are plotted as a function of β for (c) parallel ($\alpha = \beta$) and (d) perpendicular ($\alpha = \beta + \pi/2$) polarization configurations. In the case of parallel polarization, the THz associated with the two shift currents retains three-fold symmetry, but is weaker as has previously been discussed. On the other hand, the emission associated with the injection current is isotropic and similar in strength to the combined shift current. Both contributions agree with theory, where only amplitudes are free parameters. In the case of perpendicular polarization, the THz associated with the shift is once again rotated with an amplitude difference of 1.8% (within noise) and weaker than its $E(\omega)$ counterpart in (b), whereas the injection current is strongly suppressed by 74%. It is predicted that suppression should be complete, because the injection current for collinear polarized $\omega + 2\omega$ excitation is aligned in the direction of the polarization. Currents perpendicular to the pump polarization may arise due to the strong spin-orbit coupling, as has been observed in other semiconductors [40], and confirmation would require a more complex model for α- and γ-dependent measurements.

Current components in the z-direction will arise from excitation at non-normal incidence, yielding other photocurrent generation mechanisms [30, 31]. Photocurrent generation may also result from a built-in electric field caused by band-bending near the surfaces [41]. The experiments performed here were unable to detect currents traveling in the z-direction, but their presence cannot be entirely ruled out. Nevertheless, the strong shift current at 2ω relies on surface (such as SS1-to-SS2 [28]) transitions and the strength of this shift current is comparable to the two-color injection current that is allowed in the bulk.

The symmetry requirement of the shift current is a result of electronic displacement along the Bi-Se bonds within the topmost layers and involving only the topological states. Examination of the experimental band structure, from Ref. [28] for example, shows that shift currents excited with ω may occur by transitions from occupied SS1 deeply below the Fermi energy to the unoccupied SS1 states just above. Linear absorption of the sample was obtained by measuring the transmission and reflection through the sample. Differential transmission ($\Delta T/T$) was also measured using a strong ω pump and weak 2ω probe, giving the two-photon absorption coefficient as $\beta_\omega(L) = \alpha_\omega(1 - \Delta T/T)/[I_p(1 - e^{-\alpha_\omega L})(1 - R^2 e^{-2\alpha_\omega L} + \Delta T/T)]$, where R is the reflection coefficient, L is the sample thickness, α_ω is the linear absorption coefficient and I_p is the pump irradiance. The absorption coefficient at ω is $\alpha_\omega = 3.6 \times 10^4$ cm^{-1}; using an irradiance of 5.6 GW/cm^2 gives an estimated bulk charge carrier density of $N_\omega = I_0(1 - R)\alpha_\omega\tau/(L\hbar\omega) = 9.25 \times 10^{19}$ cm^{-3}, where τ is the pulse duration, R is the reflectivity, I_0 is the irradiance and L is the interaction thickness, which is set to ~3 nm for surface photocurrents based on a value determined in a bulk sample [31]. It is assumed that contributions to the photocurrent predominantly come from the Bi$_2$Se$_3$ surface that the laser pulses impinge upon, due to a rapid reduction of the two-photon absorption coefficient (data not shown). Estimates of carrier density are an upper limit of the carriers that contribute to the surface current, because α_ω is measured for the entire Bi$_2$Se$_3$ layer and includes bulk absorption. In comparison, excitation at 2ω allows for transitions between SS1 and SS2 Dirac cones, where the transition matrix elements are greater [28]. In this case, the absorption coefficient $\alpha_{2\omega} = 7.0 \times 10^6$ cm^{-1} is stronger and an irradiance of 1.1 GW/cm^2 produces a bulk carrier density of 2.19×10^{20} cm^{-3}. The two one-color photocurrents have maximum THz signals of 7 μV (350 kV/cm) for ω and 1.9 μV (95 kV/cm) for 2ω. Normalization to the respective irradiance of each pump shows that the 2ω shift current is 36% stronger, possibly due to allowed SS1-SS2 transitions.

On the other hand, the THz signal associated with the total shift current, produced in the presence of both pump pulses, is the same strength as for ω alone, namely 7 μV (350 kV/cm). Normalized to the total pump irradiance, this result is weaker by approximately 20%, due to the
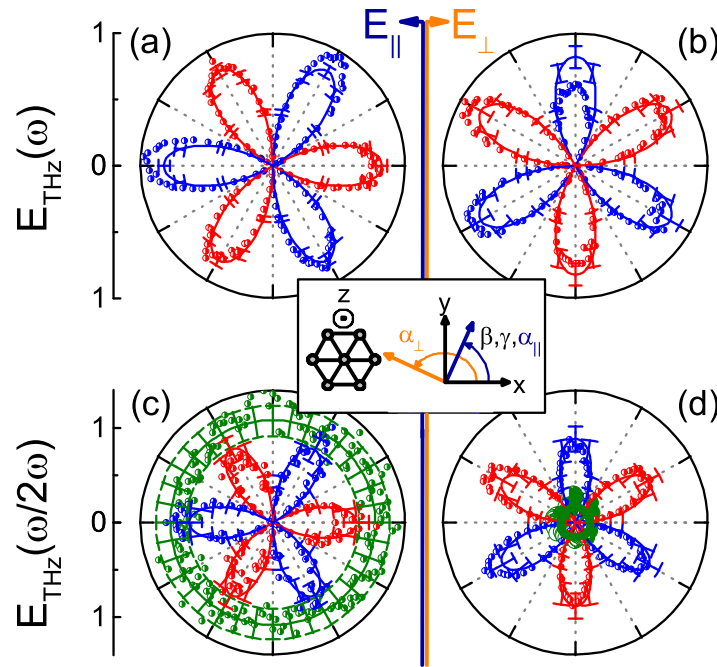
Fig. 5. One- and two-color photocurrents. Maximum THz emission (at $t_{det} = 0$) versus β are plotted for (a) parallel ($\alpha = \beta$) and (b) perpendicular ($\alpha = \beta + \pi/2$) polarization configurations, capturing the shift current due to ω excitation (blue for positive, red for negative). The solid lines are Eq. (2) with amplitudes as free parameters. Relevant angles are shown in the inset. Two-color experiments revealing the shift (blue and red) and injection (green) current, extracted using Eq. (6) are plotted for (a) parallel and (b) perpendicular polarization configurations. All data have been normalized to the magnitude of $E_{\parallel}^{shift}(\omega)$.

free-carrier absorption of the THz radiation. Additionally, the signal strength associated with the total shift current is similar to that extracted for the two-color injection current. This result is unusual, because in most semiconductors the injection current is stronger than the shift current [18]. In this case, the topological protection of the surface states may cause the observed situation. The total charge carrier concentration for the two-color photocurrent is 2.28×10^{20} cm^{-3}, estimated using $\alpha_{2\omega}$ and the measured two-photon absorption, $\beta_{\omega} = 6.5 \times 10^4$ cm/GW, and considering the reduction in the ω pulse due to one-photon absorption. In comparison, the carrier concentration that potentially contributes to the total shift current is a little higher, at 3.12×10^{20} cm^{-3}, based on the bulk absorption coefficients. The spatial restrictions on the surface one-color currents versus the bulk two-color currents would at least limit the contributing carrier concentration in the surface shift currently by a factor of 2 or 3. Therefore, having similar strengths of THz signals is an indication that acceleration of surface charge carriers contribute to the emission more significantly. This result may be attributed to slower response of bulk carriers and their currents compared with that of surface carriers [42, 43] and is consistent with the expected reduction of SS scattering [1].

Finally, the absolute strength of the injection current in Bi$_2$Se$_3$ is compared to a prototypical system for such studies, namely a 1-μm-thick crystal of GaAs using the same excitation conditions. Absorption coefficients in GaAs, measured the same way as those above for Bi$_2$Se$_3$, are $\alpha_{2\omega} = 1.5 \times 10^4$ cm^{-1} and $\beta_{\omega} = 5.0$ cm/GW, such that the total carrier concentration via both single- and two-photon absorption is 1.6×10^{15} cm^{-3}. Both the two-photon absorption and

the total injected carrier density are significantly weaker than in Bi_2Se_3, in part due to the large difference in band gap. However, the measured THz signals have similar strength. As a result, only thin films of TIs are required to rival wider-gap semiconductor crystals for generation of THz radiation via any of the observed photocurrent mechanisms.

4. Conclusions

Photocurrents are often used as tools for exploring interesting optoelectronic properties of semi-conductors. In many systems, selection rules and sample geometry preclude some photocurrent mechanisms while allowing others. Although in certain cases both one-color and two-color photocurrents have been observed simultaneously, to date they have not been isolated and studied in-depth in a rich system like the distinctive bulk and surface state energy bands in three-dimensional topological insulators. Adding and subtracting photocurrent contributions acquired from separate one- and two-color measurements was shown to have limitations coming from interplay between the two pulses even outside the cross-correlation envelope. Here an all-optical coherent control method is exploited to isolate the total shift current arising from two one-color excitations and the two-color injection current generated through quantum interference. It is shown that a relative-phase and polarization dependence analysis of the two-color measurement allows for extraction of the total shift current in the presence of free-carrier absorption.

Comparison of these measurements with theoretical predictions gives information about the origins of each photocurrent. The dependence on the direction of the polarization of the incident fields and their relative strengths suggest that the shift currents arise from surface-to-surface transitions where possible. The resulting emission is comparable to that for the bulk injection, which is expected to be stronger in a near-perfect material. These contributions indicate that surface charges are more responsive to the optical stimulation. Additionally, both one- and two-color photocurrents in thin films of materials such as Bi_2Se_3 appear to be better emitters of THz radiation than GaAs and similar semiconductors crystals.

This all-optical strategy can potentially provide insight into the optoelectronic properties of TIs, as well as infer transport characteristics that can not be easily measured in measurements with contacts. By exploring different parameters such as sample thickness, optical wavelengths, or detecting spin-polarization by probe experiments [44], the electronic and spintronic character-istics of excited states (including this in SS2) could be mapped out explicitly. Thus, this tool for isolating the photocurrents can bridge results from angle-resolved photoemission spectroscopy and transport measurements in materials with similarly rich physical properties. This techniques may be applied to topological surface states that have not yet been confirmed, or materials that also exhibit generation of multiple and simultaneous photocurrents, and in any material or devices where non-invasive measurement is essential.